Available online at www.sciencedirect.com
SCIENCE DIRECT®
International Journal of Heat and Mass Transfer 48 (2005) 2635–2651
International Journal of HEAT and MASS TRANSFER
www.elsevier.com/locate/ijhmt

Analysis of pulsating heat pipe with capillary wick and varying channel diameter

Brian Holley, Amir Faghri *

Department of Mechanical Engineering, University of Connecticut, Storrs, CT 06269, United States

Received 22 December 2004; received in revised form 31 January 2005
Available online 28 March 2005

Abstract

Variation in channel diameter is investigated as a means of enhancing heat transfer in a pulsating heat pipe with capillary wick using the model presented here. The model is one-dimensional with slug flow where the momentum equation is solved for each liquid slug. The number and mass of liquid slugs are allowed to vary throughout a simulation. The energy equation is solved both in the wall and wick and in the working fluid. The effects of diameter profile, gravity, fill ratio, and heating and cooling schemes can be studied with the model. Results yield similar trends to what has been experimentally observed. Results also indicate that heat transfer can be enhanced when the diameter of the channel is varied along the channel length, thereby providing increased range of heat load capability, less sensitivity to gravity, and in some cases smaller temperature differentials.

1. Introduction

Pulsating heat pipes (PHPs) transfer heat due to movement of liquid slugs and vapor plugs along a conduit. Liquid slugs and vapor slugs, shown in Fig. 1, occupy alternating portions of the conduit or channel. Slugs and plugs meet at liquid–vapor interfaces called menisci. Unlike in a conventional heat pipe, liquid and vapor in PHPs must move together if the menisci are to remain intact. Although the configuration can vary, a typical PHP consists of parallel channels connected by turns forming an elongated serpentine loop, as shown in Fig. 1. Portions of the loop comprise the heating (evaporator) sections, cooling (condenser) sections, and adiabatic sections.

When a PHP operates successfully, vapor plugs continually grow and shrink. Plug growth occurs due to boiling, evaporation, and density change caused by temperature variation. Plugs shrink due to condensation as well as density change. The resulting fluid movement provides the momentum or uneven hydrostatic pressure needed to move other slugs or plugs to locations where evaporation, boiling, condensation and change in vapor density can occur. The impetus provided by evaporation, boiling and condensation needs to overcome viscous damping by the fluid and adverse body forces (e.g., gravity pulling liquid away from the heating section), otherwise fluid movement and performance will not be sustained.

Interest in PHPs comes from the high heat flux capability observed for some prototypes. High heat flux over a low temperature differential with a passive device is

* Corresponding author. Tel.: +1 860 486 2221; fax: +1 860 486 0318.
E-mail addresses: bmholley@engr.uconn.edu (B. Holley), faghri@engr.uconn.edu (A. Faghri).

0017-9310/$ - see front matter © 2005 Elsevier Ltd. All rights reserved.
doi:10.1016/j.ijheatmasstransfer.2005.01.013

Nomenclature

a, b	integration limits
A	cross sectional channel area, m^2
C_S	Simpson quadrature partial sum
C	Fanning friction factor
C_t	time step refinement factor
C_p	specific heat, J/kg K
d	channel diameter, m
F	Simpson quadrature iteration
g	gravity acceleration, m/s^2
h	heat transfer coefficient, W/m^2 K
H	enthalpy, J/kg
i	slug index
k	summation index or thermal conductivity, W/m K
k_s	surface roughness feature size, m
L	length along flow path, m
m	mass, kg
$\dot{m}$	mass flow rate, kg/s
n	summation index
n_{pt}	number of parallel tubes
n_s	number of liquid slugs
N	summation limit
Nu	Nusselt number, hd/k_ℓ
p	perimeter, m
P	pressure, Pa
Pr	Prandtl number
Q	heat rate, W
q	heat flux rate, W/m^2
r	capillary radius, m
Re	Reynolds number, $\dot{m}d/\mu_\ell A$
R	gas constant, J/kg K
t	time, s
T	temperature, K
u	velocity, m/s
V	volume, m^3
z	axial location, m

Greek symbols

γ	ratio of liquid volume to channel volume
δ	thickness, m
Δ	increment of
ε	wick porosity
θ	angle between gravity vector and z coordinate, rad
μ	absolute viscosity, Pa s
ρ	density, kg/m^3
σ	surface tension, N/m
τ	shear, Pa
ϕ	wick porosity

Subscripts

b	back or boiling
c	condenser
e	evaporator
ex	external
f	front or fluid
g	gas (Vapor)
i	slug index
ℓ	liquid
o	residual
p	plug
s	sensible
sat	saturated
t	total
w	wall
wk	wick
∞	ambient

desirable for electronics and laser cooling. Channel walls lined with a porous metal wick have augmented the performance of PHPs. About one-tenth of the temperature differential is required to produce the same boiling heat flux from a sintered metal surface than from a smooth metal surface [1]. Heat fluxes of over 200 W/cm^2 at a temperature difference of just 20 K have been reported for PHPs with sintered porous wicks [2].

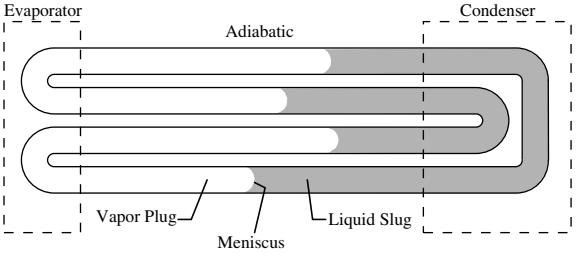

Fig. 1. Schematic of a pulsating heat pipe with four parallel tubes.

Flow visualization studies have shown that flow inside a PHP can be random, oscillatory, and circulatory [3,4]. Oscillating flow is the cyclic movement of liquid slugs in one direction and then another. Net fluid flow in one direction is circulatory flow. It occurs only with looped PHPs, but it is not always sustained at steady state operation. Circulatory flow may be desirable, however, if it results in greater sensible heat transfer. The idea is based on the prediction that more sensible heat transfer occurs than latent heat transfer [5]. In this case the role of latent heat transfer is to provide movement to the liquid

slugs. Khandekar and Groll [4] provide very good descriptions of the oscillation and circulation phenomena in a PHP. Oscillation gives way to circulation as heat load is increased. Circulation occurs in one direction for an unspecified time, possibly followed by a flow reversal.

Design and implementation of PHPs would be simplified if the flow inside were predictable and sustained. To confront this issue, in his patent Akachi [6] did claim that PHPs may be configured in such a way that the flow is sustained and circulatory by the addition of check valves, but no reports have been published on the performance of such a device.

Asymmetric flow resistance and capillarity can also assist fluid movement. A bubble in an expanding tube (gradually increasing in diameter) will have a net force acting in the expanding direction because of uneven capillary forces. As movement ensues, the lower flow friction in the direction of the expansion further influences the fluid flow. The concept of varying capillarity has been applied to a pump with no moving parts [7] where Joule heating of the fluid causes vapor bubble growth and liquid pumping in the expanding tube direction against a pressure head of 2–3 cm. Although it is dependent on the density and surface tension properties of the liquid being used, the maximum tube diameter for such a pump is generally a few millimeters, above which the bubble can fail to sufficiently block the tube.

The objective of this work is to develop a model that can be used to study a PHP with sintered porous wick and investigate the benefits of varying the channel diameter along the flow path. What is sought is a heat pipe that exhibits the high heat flux capability that has been reported with a sintered wick, but with the added characteristic that the flow inside is circulatory.

2. Analysis

In the modeling domain the channel is considered as one straight flow path with the end conditions set equal. The diameter is a design parameter, and is defined as a function of length along the flow path. Fill ratio is also a design parameter. The angle between the gravity vector and the channel axis is an operating condition and a function of location. Various sections of the flow path comprise the evaporator, adiabatic and condenser sections. Assumptions are stated as follows.

(1) Derivatives of density and viscosity are assumed negligible in order to simplify the analysis with regard to the momentum equation. However, density and viscosity are evaluated as functions of temperature in the simulation.
(2) The mass flow rate of each liquid slug is constant along its length at a given time.
(3) The model is one-dimensional, with the axial dimension along the flow path considered for momentum and heat transfer; heat transfer transverse to the flow path is lumped.
(4) The menisci of the liquid slugs are assumed to maintain a spherical meniscus shape with zero contact angle at the wall.
(5) Surface tension is evaluated at the plug temperature.
(6) The effect of the turns is neglected.
(7) The pressure within each vapor plug is assumed uniform.
(8) Vapor exists at saturated conditions.
(9) There is negligible flow friction corresponding to the vapor plugs.

The change in mass flow rate and locations of the menisci for each liquid slug are determined by accounting for momentum balance explicitly in time. To clarify the derivation, a slug will be illustrated and the nomenclature explained. The pressures acting on the liquid slug will then be described followed by the rate of momentum change of the slug.

Now the liquid slug as applied to the model will be described. Fig. 2 is a schematic of an arbitrary ith slug. Variables associated with the ith slug are written with a subscript (ℓ). The liquid slug has a back meniscus and front meniscus, the locations of which are indicated. Variables associated with the front and back menisci have subscripts as shown in the figure. The back and front menisci also have corresponding velocities. Channel diameter is shown as a function of location.

From the equation for rate of momentum change, the rate of change in mass flow rate is determined. The momentum equation for incompressible flow in a circular pipe is

$$\rho \frac{Du}{Dt} = \rho g \cos\theta - \frac{\mathrm{d}P}{\mathrm{d}z} + \frac{4\tau}{d} \tag{1}$$

Note that θ describes the angle between the gravity vector and tube axis. A null angle means gravity is acting in the $z+$ direction. Mass flow rate can be substituted for velocity by $\dot{m} = \rho u A$. With Assumption 2 the axial derivative of mass flow rate is zero along each liquid

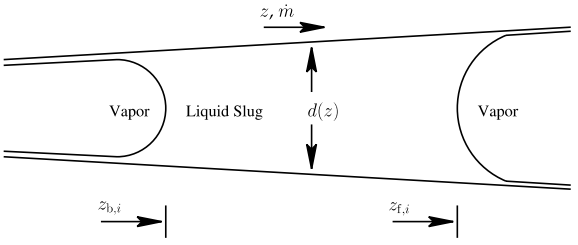

Fig. 2. Schematic of a liquid slug in the PHP model.

slug, and with Assumption 1 time and axial derivatives of density are zero. Eq. (1) is integrated from the back meniscus to the front meniscus

$$\frac{\mathrm{d}\dot{m}}{\mathrm{d}t}\int_{\mathrm{b}}^{f}\frac{1}{A}\mathrm{d}z+\frac{\dot{m}^2}{2}\left[\frac{1}{(\rho A^2)_{\mathrm{f}}}-\frac{1}{(\rho A^2)_{\mathrm{b}}}\right]=\int_{\mathrm{b}}^{f}\rho g\cos\theta\mathrm{d}z-(P_{\mathrm{f}}-P_{\mathrm{b}})+4\int_{\mathrm{b}}^{f}\frac{\tau}{d}\mathrm{d}z \tag{2}$$

The first and second terms on the left hand side are pressure differences due to acceleration as a result of mass flow rate change and dilatation (slug elongation or shortening) respectively. The terms on the right hand side refer to the hydrostatic pressure difference, difference between pressures at the slug menisci, and pressure difference due to shear.

There are two components to the pressure at the end of a liquid slug. One component is the vapor pressure, which is assumed to be at the saturation pressure at the temperature of the vapor plug per Assumptions 7 and 8. The second component is the pressure rise across the meniscus surface due to capillary pressure, the radius for which is dependent on axial location.

$$(P_{\mathrm{f}}-P_{\mathrm{b}})=\left[P_{\mathrm{sat}}(T)-\frac{2\sigma}{r}A\right]_{\mathrm{f}}-\left[P_{\mathrm{sat}}(T)-\frac{2\sigma}{r}A\right]_{\mathrm{b}} \tag{3}$$

The shear term in Eq. (2) is treated semi-empirically. The flow is considered to be either fully developed laminar or turbulent. Local values of shear along the ith slug are determined for Hagen–Poiseuille (exact) flow or for turbulent flow (empirical) in a rough pipe. For turbulent flow roughness is considered as a result of the wick. The size of a powder particle for a sintered powder wick, or a capillary pore for a sintered filamentary wick, is chosen as the size for the roughness features. The Colebrook correlation accounts for surface roughness and is used for turbulent flow [8].

$$\tau=\frac{1}{2}C\rho u^2=\frac{C\dot{m}^2}{2\rho A^2}$$

with

$$\begin{cases} C=\dfrac{16}{Re} & Re<2000 \\ \dfrac{1}{2\sqrt{C}}=1.74-2.0\log\left(\dfrac{2k_{\mathrm{s}}}{d}+\dfrac{18.7}{2Re\sqrt{C}}\right) & Re\geqslant 2000 \end{cases} \tag{4}$$

Temperature in the fluid and wall is determined by accounting for energy balance. The energy equation is applied individually to the wall and wick, liquid slugs, and vapor plugs. The three energy equations are coupled by convective heat transfer terms with appropriate heat transfer coefficients. Latent and sensible heat transfer occur between the tube wall and fluid. Boiling, evaporation, and condensation comprise latent heat transfer. Sensible heat transfer occurs by conduction or convection with laminar or turbulent flow. Within the liquid slugs heat is conducted in the axial direction. Because of the uniform temperature assumed in each vapor plug, convection occurs implicitly in the axial direction. Heat transfers also from the vapor plugs to the slug menisci. Within the tube wall heat is allowed to conduct in the axial direction. On the tube exterior constant heat input per unit length is applied at the evaporator. Convection occurs to some constant exterior temperature with a constant heat transfer coefficient in the condenser section. No heat transfer occurs over the remainder of the exterior (i.e., adiabatic section).

The energy balance for the wall is based on heat flow within the wall and heat transfer to and from the fluid, evaporator and condenser. The wick and wall are lumped in the energy balance

$$\{C_{\mathrm{p,w}}\rho_{\mathrm{w}}[A_{\mathrm{w}}+(\varepsilon-1)A_{\mathrm{wk}}]+C_{\mathrm{p},\ell}\rho_\ell\varepsilon A_{\mathrm{wk}}\}\frac{\partial T_{\mathrm{w}}}{\partial t}=q_{\mathrm{ex}}p_{\mathrm{o}}-q_{\mathrm{w-f}}p-(k_{\mathrm{w}}A_{\mathrm{w}}+k_\ell A_{\mathrm{wk}})\frac{\partial^2 T_{\mathrm{w}}}{\partial z^2} \tag{5}$$

The outer wall perimeter is $p_{\mathrm{o}}=\pi(d+2\delta_{\mathrm{w}}+2\delta_{\mathrm{wk}})$. External heat transfer depends upon location along the flow path. In the evaporator the external heat input is a constant heat flux. In the adiabatic section there is no heat transfer to the exterior, and in the condenser, the heat rate is based on a constant convection coefficient to the exterior ambient temperature.

$$q_{\mathrm{ex}}=\begin{cases} q_{\mathrm{e}} & \text{Evaporator} \\ 0 & \text{Adiabatic} \\ h_\infty(T_{\mathrm{w}}-T_\infty) & \text{Condenser} \end{cases} \tag{6}$$

The energy balance for the liquid is based on heat conduction within the fluid and heat transfer to and from the wall. The formulation is Lagrangian, and there is no axial convection

$$C_{\mathrm{p},\ell}\rho_\ell A\frac{\partial T}{\partial t}=pq_{\mathrm{w-f}}-k_\ell A\frac{\partial^2 T}{\partial z^2} \tag{7}$$

Heat transfer in the vapor plugs is expected to be much greater than heat transfer in the liquid, so it is lumped. Fig. 3 shows heat storage and heat flow into and out of a control volume comprising an arbitrary vapor plug. The differential formulation of the energy equation for lumped heat transfer in the vapor plug is

$$\frac{\partial}{\partial t}\left(H_{\mathrm{g}}\frac{P}{RT}\int_{z_{\mathrm{f},i-1}}^{z_{\mathrm{b},i}}A\mathrm{d}z\right)=\int_{z_{\mathrm{f},i-1}}^{z_{\mathrm{b},i}}pq_{\mathrm{w-f}}\mathrm{d}z-k_\ell A\left.\frac{\partial T}{\partial z}\right|_{z_{\mathrm{f},i-1}}+k_\ell A\left.\frac{\partial T}{\partial z}\right|_{z_{\mathrm{b},i}} \tag{8}$$

The heat transfer coefficient between the fluid and wall is based on experimental data and an empirical correlation. Heat transfer between the wall and vapor plugs occurs as boiling, evaporation, and condensation.

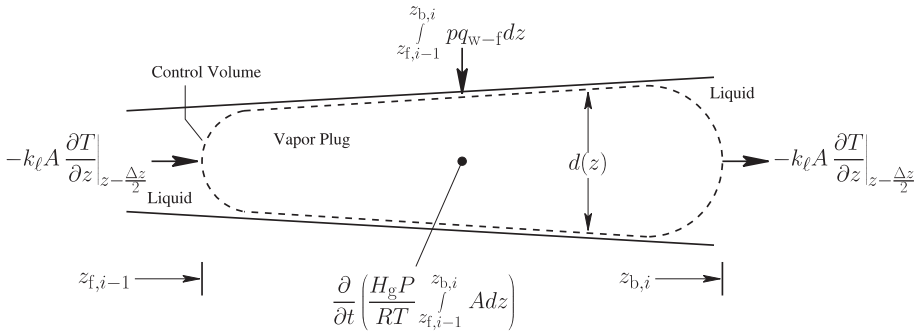

Fig. 3. Heat storage and flow into and out of a control volume comprising a vapor plug.

Evaporation occurs at the surface of the saturated wick, and boiling occurs closer to the tube wall within the wick. The mode of vaporization depends on the temperature difference between the wall and fluid. The heat flux from the wall to the fluid is

$$q_{w-f} = h(T_w - T_f) \tag{9}$$

The boiling heat transfer coefficient is applied under certain conditions to heat transfer from the wall to the fluid, whether it be vapor or liquid. Webb [1] reports a comparison in boiling heat flux for smooth and porous metal surfaces. The temperature difference required to produce a given heat flux is reduced by a factor of 10 for pool boiling of water on a porous rather than a smooth metal surface. The temperature difference is that between the wall and liquid saturation temperature. To apply the data reported by Webb to a boiling heat transfer coefficient for the present model, a linear fit is computed from those data

$$h_b = [213(T_w - T_f) - 80.4] \times 10^3 \text{ W/m}^2 \text{ K} \tag{10}$$

The boiling heat transfer coefficient applies when it exceeds the evaporation or sensible heat transfer coefficients. Evaporation and condensation occur between the liquid layer in the wick and a vapor plug. The same heat transfer coefficient is used for both evaporation and condensation, and it is based on the thickness and conductivity of the wick as saturated with working fluid. Measurements of heat transfer coefficients for water undergoing complete condensation by Begg et al. [9] indicated that the primary mode of heat transport was conduction through a liquid film on the tube wall for water in tube diameters consistent with the PHPs modeled here. In the current study, the presence of the wick will lead to an even thicker and slower moving liquid layer than the film in the condensation experiments. It is expected that modes of heat transfer other than conduction through the liquid layer will be negligible. The evaporation and condensation heat transfer coefficient through the liquid layer is $h_{c,e} = k_{wk}/\delta_{wk}$. The effective conductivity of the wick for various wick types can be found in Faghri [10].

For sensible heat transfer to laminar flow the Nusselt number is assumed a constant 4.36 for fully developed flow with constant heat flux. Under certain conditions Nusselt numbers vary from 3.66, for fully developed laminar flow with an isothermal wall, to over 40 for the hydrodynamic entrance region of a tube with constant heat flux. In the present study the temperature and velocity profiles in the fluid are unknown, so the assumption is made for fully developed laminar flow subject to constant heat flux.

For sensible heat transfer to turbulent flow the roughness of the wick is taken into account. The Gnielinski correlation applies a friction factor that varies with roughness. The Colebrook correlation used in Eq. (4) provides the needed friction factor. Reynolds and Prandtl numbers are taken at local flow conditions along with the friction factor for the Gnielinski correlation [11]

$$Nu = \frac{(C/2)(Re - 10^3)Pr}{1 + 12.7(C/2)^{1/2}(Pr^{2/3} - 1)} \tag{11}$$

which is stated to hold for $0.5 < Pr < 10^6$ and $2300 < Re < 5 \times 10^6$. For this study the Gnielinski correlation will be applied for $Re \geqslant 2000$. The sensible heat transfer coefficient, along with conduction through the wick is analogous to the sum of two resistances in parallel

$$h_s = \left[\frac{\delta_{wk}}{k_{wk}} + \frac{Nu\,d}{k_\ell}\right]^{-1} \tag{12}$$

3. Numerical procedure

First, several design and computational parameters and operating and initial conditions are defined.

1. Design parameters:
   (a) Channel: fill ratio, length, surface roughness feature size, and diameter as a function of length.

(b) Wall: density, specific heat, thermal conductivity, thickness, wick thickness, wick thermal conductivity.

2. Computational parameters: maximum time step, minimum time step refinement factor, convergence criterion, trapezoidal integration length step, maximum allowable plug temperature change between time steps, and simulation time. In order to handle derivatives, the wall and each liquid slug are represented by one-dimensional computational grids. The grids for the liquid slugs are allowed to move. The number of grid nodes comprising wall and liquid are specified here as well.
3. Operating conditions: ambient temperature, condenser heat transfer coefficient, initial temperature, total heat input rate, and functions of length: evaporator, adiabatic and condenser locations and gravity angle.
4. The Nusselt number for laminar slug flow is set for the simulation.
5. Initial conditions:
   (a) The liquid begins as one slug, and time, mass flow rate and pressure differentials on the slug are set to zero.
   (b) The total internal volume of the heat pipe is calculated by trapezoidal integration. The length step Δz from Step 2 and N are iteratively increased until the condition below is satisfied.

$$V_t = \frac{\Delta z}{2}\sum_{n=1}^{N}\{A[(n-1)\Delta z] + A(n\Delta z)\} \times \frac{\Delta z_o}{2}[A(L-\Delta z_o) + A(L)]$$

such that $L = N\Delta z + \Delta z_o$, and $\Delta z_o < \Delta z$.

   (c) The initial positions of the menisci are calculated by integration in the manner of Step (b). $z_b = 0$ and

$$z_f = N\Delta z + \Delta z_o, \quad \text{such that } \Delta z_o < \Delta z \text{ and}$$

$$\frac{\Delta z}{2}\sum_{n=1}^{N}\{A[(n-1)\Delta z] + A(n\Delta z)\} + \frac{\Delta z_o}{2}[A(N\Delta z - \Delta z_o) + A(N\Delta z)] = \gamma V_t$$

   (d) The mass of the slug is integrated using area as a function of length and liquid density as a function of temperature.

$$m = \frac{\Delta z}{2}\sum_{n=1}^{N}\{(\rho A)[z_b + (n-1)\Delta z] + (\rho A)(z_b + n\Delta z)\} + \frac{\Delta z_o}{2}[(\rho A)(z_f) + (\rho A)(z_f - \Delta z_o)]$$

such that $z_f - z_b = N\Delta z + \Delta z_o$, and $\Delta z_o < \Delta z$.

Several quantities are integrated in the following steps. For this purpose adaptive Simpson quadrature is applied. The integral is approximated to the nth iteration as

$$\int_b^a f(z)\,dz \approx \frac{1}{3}F_n \tag{13}$$

The following relations close the definition

$$F_n = \frac{1}{2}\left[F_{n-1} + \frac{2C_n - C_{n-1}}{2^{n-2}}\right], \quad F_0 = f(a) + f(b)$$

$$C_0 = 0, \quad C_n = \sum_{k=1}^{2^{n-1}} f\left\langle a + \frac{\langle b-a\rangle(2k-1)}{2^n}\right\rangle$$

The brackets $\langle\,\rangle$ denote a function that allows for circulation and is defined as

$\langle z\rangle = z + L \quad z < 0$

$\langle z\rangle = z - L \quad z > 0$

$\langle z\rangle = z \quad$ otherwise

The quadrature is iterated for increments of n, and when results from two subsequent iterations agree within the convergence criterion, the latter value is taken as the integral.

   (e) The evaporator heat flux is calculated based on the total heat input rate and combined evaporator section length

$$q_e = Q_e\left[\int_0^L p\begin{Bmatrix}1 & \text{evaporator}\\ 0 & \text{otherwise}\end{Bmatrix}dz\right]^{-1}$$

   (f) Locations of grid boundaries in the liquid slugs are determined. Slugs are represented by a number of equal mass increments. The rear boundary of the first mass increment in each slug is the back meniscus. The forward boundary is located using the secant method. The first two points for the secant method are $z' = z_b$ and $z' = \langle z_b + m/n_s\rho A\rangle$ with $m' = \int_{z_b}^{z'}\rho A\,dz$. Subsequent values of z' are obtained using the secant method. The value of the forward boundary is taken when $[n_s m'(z') - m]/m$ satisfies the convergence criterion. The representative location for each grid is taken as the midpoint between the grid boundaries. Density is evaluated at the temperature found by linearly interpolating adjacent grid values.

Forward and backward extrapolation is used near the menisci where points do not lie between the representative locations of two adjacent grids. Area is a function of location as indicated in Step 1a. The location of the forward meniscus is set equal to the forward boundary of the last mass increment.

(g) The volumes of the vapor plugs are calculated by $V_{p,i} = \int_{z_{f,i-1}}^{z_{b,i}} \rho A \, dz$. The time iteration loop begins here.

6. The time step refinement factor is determined. If a collision between adjacent slugs is anticipated before the next time step, the time step is reduced to synchronize the collision with the next time step, which serves to reduce overlap of the menisci.

$$C_{t,i} = \frac{\langle z_{b,i} - z_{f,i-1} \rangle}{\Delta t \left[\left. \frac{\dot{m}}{(\rho A)_f} \right|_{i-1} - \left. \frac{\dot{m}}{(\rho A)_b} \right|_{i} \right]}$$

7. The differential pressure due to gravity across each slug is determined as indicated in Eq. (2).
8. The differential pressure across each slug due to shear is calculated per Eq. (2) and (4).
9. The incremental change in mass flow rate is calculated using Eq. (2) with the results of the previous three steps.
10. The displacements of the back menisci positions are calculated based on mass flow rate and time step by convergence of the following equation

$$\Delta z_i = \frac{\Delta t}{2} \left(\frac{\dot{m} + \Delta \dot{m}}{\rho[T\langle z_{b,i} + \Delta z_i \rangle] A \langle z_{b,i} + \Delta z_i \rangle} + \frac{\dot{m}}{\rho[T(z_{b,i})] A(z_{b,i})} \right)$$

The initial estimate to the above equation is

$$\Delta z_i = \frac{\Delta t}{2} \left(\frac{\dot{m} + \Delta \dot{m}}{\rho[T(z_{b,i})] A(z_{b,i})} \right)$$

The back meniscus position is updated as $z_{b,i} = \langle z_{b,i} + \Delta z_i \rangle$.

11. Slug grid boundaries and the front slug menisci are located as done in Step 4f.
12. Heat transfer from the wall to the fluid at each wall grid is determined using Eq. (9).
13. The temperature for each wall grid is evaluated by integrating Eq. (5) along the grid length. The remaining spatial derivative is determined using a first order central difference. Values of heat transfer between the wall and fluid are interpolated based on the representative values of adjacent grids.
14. The temperature of the vapor plugs is determined using Eq. (8). Heat transfer values from the wall to fluid are interpolated. For the spatial temperature derivatives, forward and backward first order differences are used for conduction at the menisci. Since temperature is a function of other values on the left hand side of Eq. (7), the equation is solved iteratively until the convergence criterion is satisfied. If the temperature change in a vapor plug from one time step to the next exceeds the allowable amount (set in Step 2), the time step refinement factor is divided by 10 and the simulation proceeds from Step 6.
15. The temperatures of the grids in each liquid slug are determined by integrating Eq. (7) along the length of each grid. For the conduction term backward, central or forward, first order differences are used based on whether the grid is a first, middle or last grid along the slug. Heat flux from the wall to the fluid is integrated with interpolated values.
16. The merging of liquid slugs is accounted for. If the spacing between any two adjacent menisci is zero, or if there is overlap, the two liquid slugs are combined and the number of liquid slugs is reduced by one. The mass flow rate for the combined slug is determined by summing the momenta.

$$\dot{m} = \frac{L_{i-1}\dot{m}_{i-1} + L_i \dot{m}_i}{L_{i-1} + L_i}$$

17. The formation of vapor plugs is accounted for. The temperature at the boundary of two grids is taken as the average temperature of the adjacent grids. That temperature is compared to the temperatures of the vapor plugs adjacent to the liquid slug. The maximum grid boundary temperature is chosen as the location where a new plug is formed if that temperature exceeds one or the other adjacent plug temperatures. The locations of the new menisci are set to that location. The mass flow rate is the same for both segments of the slug. The temperature of the plug is set to the fluid temperature at that location. Another criterion for locating new vapor plugs is to compare the saturation pressure associated with the grid boundary temperature to the pressure of the grid boundary as

Table 1
Parameters general to all cases

Initial and ambient temperature	$T = T_\infty = 303.15$ K
Tube roughness feature size	40 μm
Wall and wick material	Copper
Wall and wick thickness	$\delta_w = \delta_{wk} = 0.5$ mm
Wick porosity	$\phi = 0.5$
Wick thermal conductivity for packed spheres [10]	$k_w = k_{Cu}\left[\frac{2 + k_\ell/k_{Cu} - 2\phi(1 - k_\ell/k_{Cu})}{2 + k_\ell/k_{Cu} + \phi(1 - k_\ell/k_{Cu})}\right]$
Working fluid	Water

computed using Eq. (2). While this may be more realistic, it was found to require too much computational time to evaluate the pressure at each grid boundary for each time step. On the other hand, if there is sufficient vapor pressure in the plug, the plug will grow, otherwise the plug will collapse again in Step 16.

18. Calculation resumes from Step 5 until the end time is reached.

4. Results

Sixteen sets for a total of 73 cases have been run to establish the computational parameters and investigate the effects of gravity, diameter profile, fill ratio, mean laminar Nusselt number, and heat load on heat transfer. The general parameters used for all cases are in Table 1. The working fluid is water, and the wick is sintered copper powder, the thermal conductivity for which is approximated by that for packed spheres. The roughness feature size used in the Colebrook correlation (Eq. (4)) is taken to be the powder particle size. Table 2 contains the parameters that may differ between cases. Case 1 is used to establish values for computational parameters to be used in the remaining cases. The next two sets of cases (2–8, 9–14) have all parameters in common except the diameter profile. The following six sets of cases (15–43) have varying diameter profiles and fill ratios to illustrate a flow map of oscillatory and pulsating circulatory flow. The three sets of cases (16, 20, 32, 44–55) show the effect of varying inclination angle on heat transfer: from −90° where the evaporator lies directly above the condenser, to 90° where the evaporator lies directly below the condenser. In the two sets of cases (56–65) the mean laminar Nusselt number is varied. The final two sets of cases (20, 32, 66–73) are included to investigate the effect of heat load.

4.1. Determination of computational parameters

The computational parameters used were established from the results of Case 1. The sensitivity was checked of

Table 2
Parameters for individual cases

Case	d, mm (range)	Inclination angle[a], °	L	L_c	L_e	n_{pt}	Q_e	γ
1[b]	2.0	90	0.250	0.040	0.020	2	20	0.60
2	1.5							
3	1.5 ± 0.1							
4	1.5 ± 0.2							
5	1.5 ± 0.3							
6	1.5 ± 0.4							
7	1.5 ± 0.5							
8	1.5 ± 0.6							
9	2.0							
10	1.8–2.0							
11	1.6–2.0							
12	1.4–2.0							
13	1.2–2.0							
14	1.0–2.0							
15:22	2.0	−90	0.750	0.120	0.060	6	60	0.65:0.30
23:28	1.9–2.0							0.55:0.30
29:33	1.8–2.0							0.50:0.30
34:38	1.7–2.0							0.50:0.30
39:41	1.6–2.0							0.40:0.30
42:43	1.5–2.0							0.35:0.30
44:47	2.0	−45:90						0.60
48:51								0.40
52:55	1.7–2.0							
56:60[c]	2.0	90						
61:65[c]	1.7–2.0							
66:68	2.0	−90					30:50	
69:71	1.7–2.0						30.50	
72:73							70:80	

[a] −90 top heat mode, 90 bottom heat mode.
[b] Variation in computational parameters.
[c] Variation in Nusselt number.

the steady state maximum wall temperature to: variations in convergence criterion, maximum plug temperature change between time steps, maximum time step minimum time step refinement factor, and spacing of grids. For one configuration of a PHP, a series of trials was run for Case 1 representing variations in each parameter.

The configuration for that PHP is described as follows, with Tables 1 and 2 showing some of the pertinent parameters. The inclination angle of the heat pipe as indicated in Table 2 is for bottom heat mode. The flow path of the heat pipe is shown in Fig. 4A. The length of the channel is 0.25 m, but for the two parallel tubes that form the loop the overall heat pipe length is about 0.125 m. The direction of gravity is indicated for 90° heat pipe inclination. Within the heat pipe the angle between the flow path and gravity varies along the flow path between 0° and 180° as shown in Fig. 4C. In Fig. 4A the evaporator is shown at the bottom and the condenser at the top. The positive axial direction is clockwise around the loop.

The simulation indicates that the fluid circulates around the loop at steady state. Fig. 5A shows the maximum and minimum wall temperatures and the total fluid momentum as a function of time throughout the three minutes simulation. The temperatures rise and level off at steady state. The total liquid momentum fluctuates between negative and positive values at first, and then settles as a negative value. It appears that as a steady state is approached and the fluid temperature increases, the momentum value further decreases, perhaps due to the reduction in viscosity. Despite the loop being symmetric, the flow circulates as indicated by the negative steady state fluid momentum. Fig. 5B shows several profiles 3 min into the simulation. Portions of the fluid temperature profile between 0.125 and 0.250 m are flat, indicating the presence of vapor plugs. Noting the location of these plugs, and referring to Fig. 4C, the buoyancy of the plugs pushes the fluid in the negative direction. As fluid approaches the evaporator, its temperature rises and new plugs form and grow, perpetuating the cycle. Due to the difference in heat transfer coefficient between boiling and condensation, the wall temperature

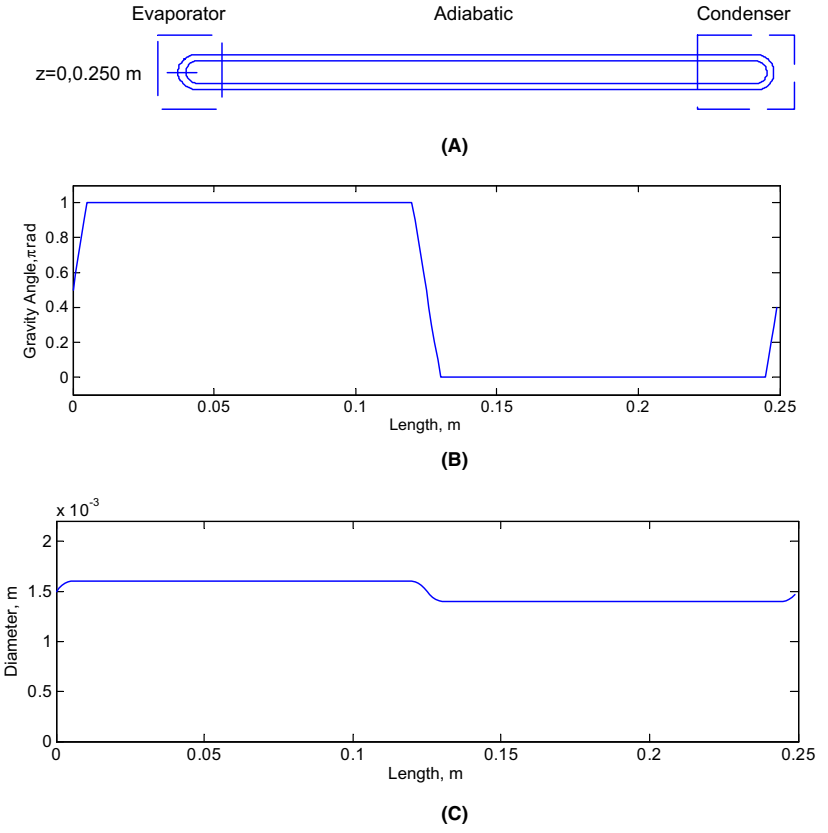

Fig. 4. Two parallel tube PHP: (A) Total length 25 cm, with 2 cm combined evaporator length, 4 cm combined condenser length, and 19 cm adiabatic; 2.0 mm diameter (Cases 1 and 9). (B) Variation of angle between channel axis and gravity with 90° inclination angle and evaporator centered at 0 m (Cases 1–14). (C) Diameter profile with a deviation of 0.1 mm from 1.5 mm mean diameter (Case 3).

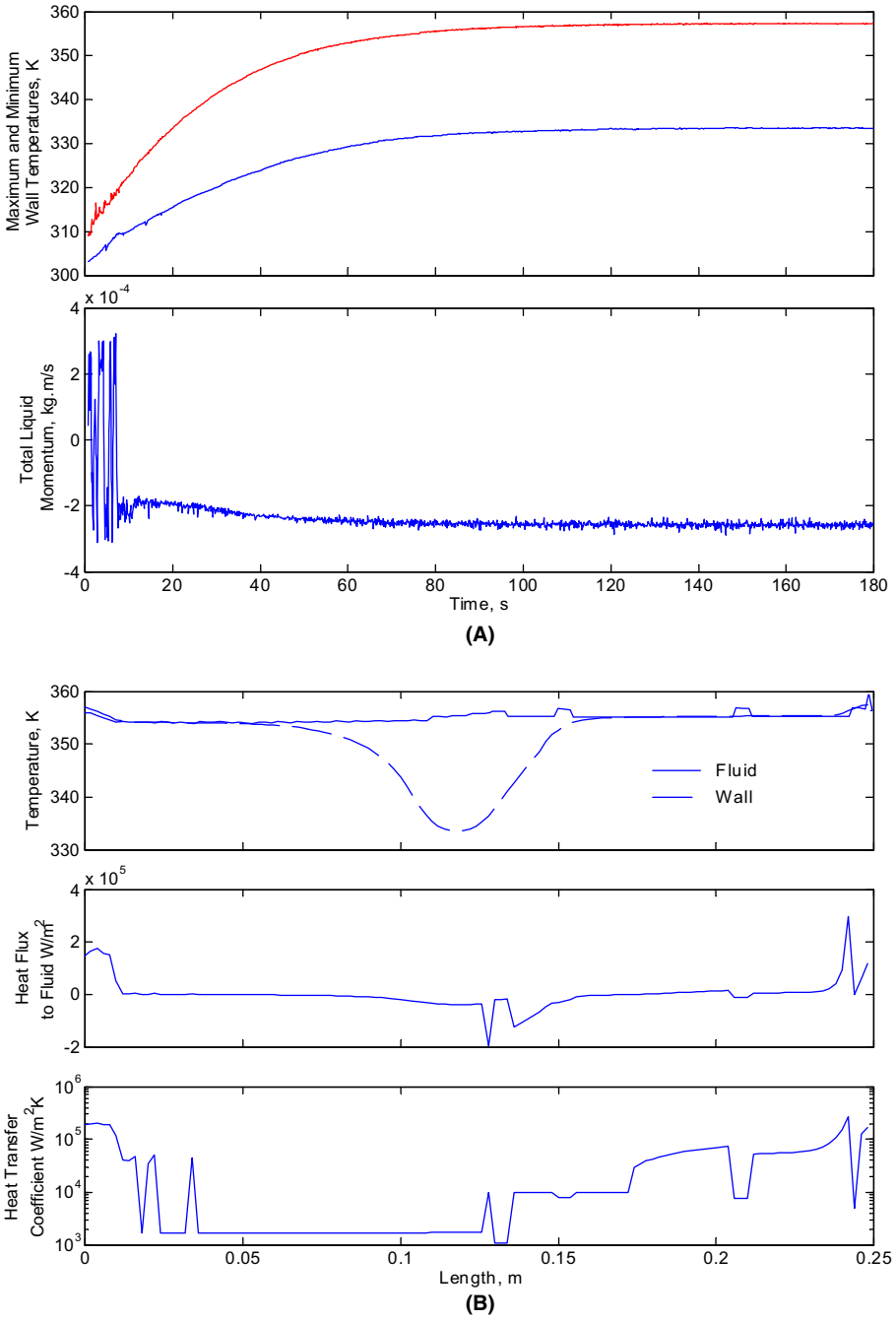

Fig. 5. Two parallel tube PHP (Case 1): (A) temperature and total liquid momentum over 180 s simulation time, and (B) profiles for wall and fluid temperature, heat flux and heat transfer coefficient 180 s into simulation.

in the evaporator is closer to the fluid temperature than to the wall temperature in the condenser. The heat flux spikes in the evaporator due to the large boiling heat transfer coefficient, and in the condenser the heat flux spikes negative with the condensation heat transfer coefficient and the relatively large temperature difference. The heat transfer coefficient stays on the order of 10^3 W/m K unless condensation or evaporation occurs.

The results from Case 1 show the sensitivity of the five computational parameters to the simulation. Ideally the results of a solution should be independent of the computational parameters used. The steady state maxi-

Table 3
Computational parameters used for Cases 2–73

Convergence criterion	1×10^{-3}
Maximum plug temperature change	10 K
Maximum time step	2×10^{-5} s
Minimum time step refinement factor	2×10^{-6}
Computational grids for wall (liquid)	$0.5L$ mm^{-1} (γL mm^{-1})

mum wall temperature is the basis of comparison chosen for sensitivity. This quantity is the average maximum wall temperature over 10 s at steady state. A sequence of values for each computational parameter is tested using Case 1. Typically each subsequent value in a sequence is one half the previous value. For example: the sequence of values tested for convergence criterion is 8, 4, 2, and 1×10^{-3}. For the computational parameter, maximum plug temperature change, five values with increments of 5 K are tested. The computational parameter values chosen for the remainder of the cases are in Table 3. For each value, and the next smaller value in its sequence, the deviation in steady state maximum temperature is less than 2 K.

4.2. Coupled buoyant and hydraulic bubble pumping

For a PHP with two parallel tubes operating in bottom heat or thermosyphon mode, the model predicts that heat transfer is enhanced when the two parallel tubes are of different diameter. The configuration for this PHP, when the diameter is constant, is similar to that reported experimentally [4]. The heat pipe modeled for Cases 2–14 is the same shown in Fig. 4A, except that the diameter of one parallel tube may be larger than the other. The evaporator and condenser lengths are the same per channel.

For the first case in the series, circulation of the working fluid is observed with a constant diameter of 1.5 mm. Fig. 6 shows the maximum and minimum wall temperatures reaching steady state while the total momentum of the liquid inside is positive, indicating circulation. The flow in the parallel tube with more liquid along its length will tend towards gravity, and the fluid in the adjacent tube with greater vapor volume will flow against gravity due to buoyancy. The fluid temperature grows as the fluid circulates first downward into and then upward out of the evaporator. Since the temperature is greater in the upward facing tube, vapor bubble growth tends to occur there, which perpetuates the flow.

The results from these cases indicate that variation in channel diameter can provide beneficial bubble pumping. According to model results, variation in the diameter along the flow path can improve performance for this configuration of PHP. For Cases 3–8 in this series, the diameter is varied. For example, Fig. 4C shows the profile of diameter with respect to length along the flow path. The diameters of the two parallel tubes are 1.4 and 1.6 mm, and each case similarly has a 1.5 mm mean diameter. The simulation for each case was run to steady state. Over the final 10 s of the simulation, where steady state is sustained, the maximum wall temperature and

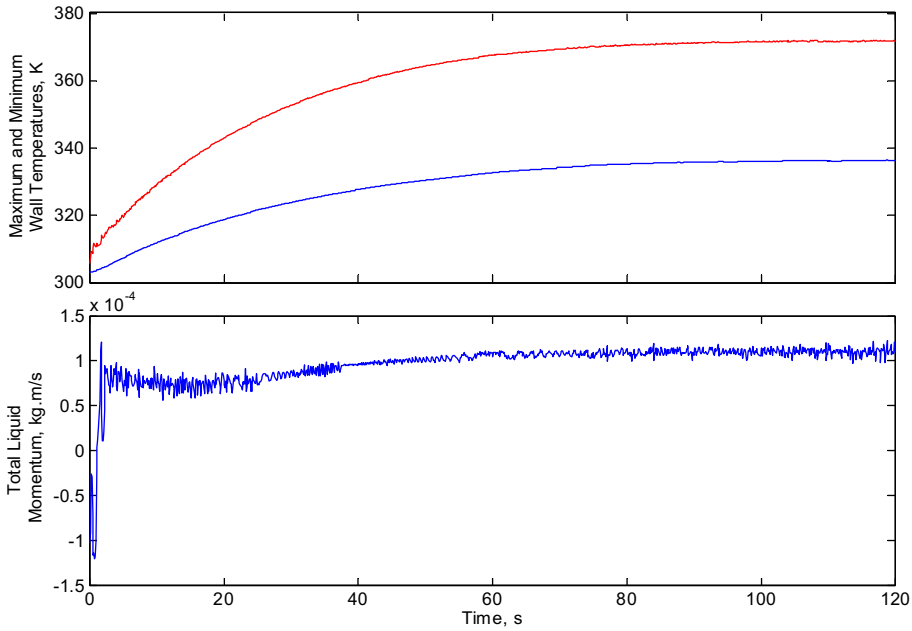

Fig. 6. Circulatory flow to steady state in a two parallel tube PHP (Case 2).

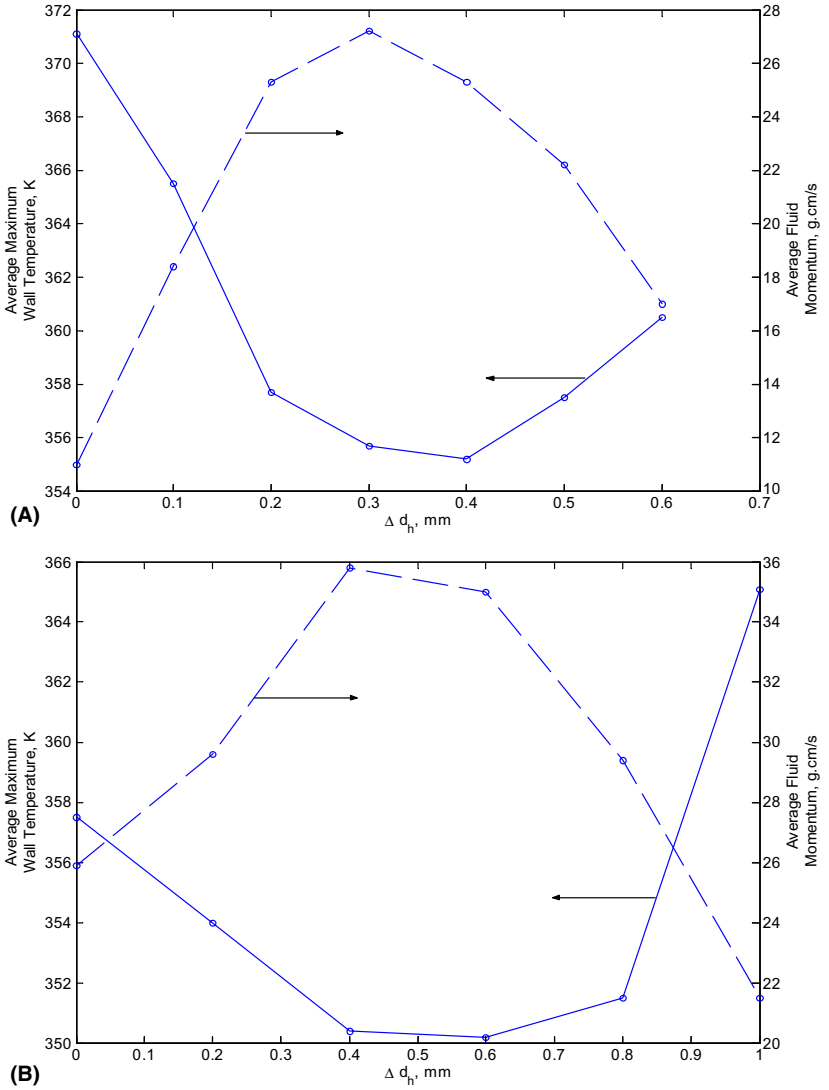

Fig. 7. Effect of varying channel diameter on maximum wall temperature and total fluid momentum for a given heat load averaged over 10 s at steady state in two parallel tube PHPs: (A) shown as deviation from 1.5 mm mean diameter (Cases 2–8); (B) one tube fixed at 2.0 mm and the other incrementally reduced from 2.0 mm by multiples of 0.2 mm (Cases 9–14).

total fluid momentum were averaged. The results with respect to deviation from mean diameter are plotted in Fig. 7A. A reduction in maximum wall temperature of 16 K is predicted when the diameter profile is changed from a constant 1.5 mm to one that varies between 1.1 mm and 1.9 mm. The reduced maximum wall temperature generally occurs with increased fluid momentum. The model predicts a point where further deviation in diameter leads to an adverse effect on maximum wall temperature, likely due to increased flow resistance in the smaller diameter tube.

A similar result is observed when one tube diameter is kept constant and the other parallel tube diameter is incrementally reduced. In Cases 9–14 one parallel tube is fixed at 2.0 mm and the other tube diameter is smaller by a multiple of 0.2 mm. The results from this set of cases are shown in Fig. 7B. A lowering in maximum wall temperature of about 7 K is seen when the diameter of one tube is reduced from 2.0 mm to 1.6 mm. In this sense, heat transfer can be enhanced even while reducing the size and volume of the device.

The model has predicted flow reversals in some cases for the two parallel tube PHP. Circulation has been observed experimentally in a similar two parallel tube PHP [4], and the circulation in the experiments was observed to periodically stop and then start again either in the same

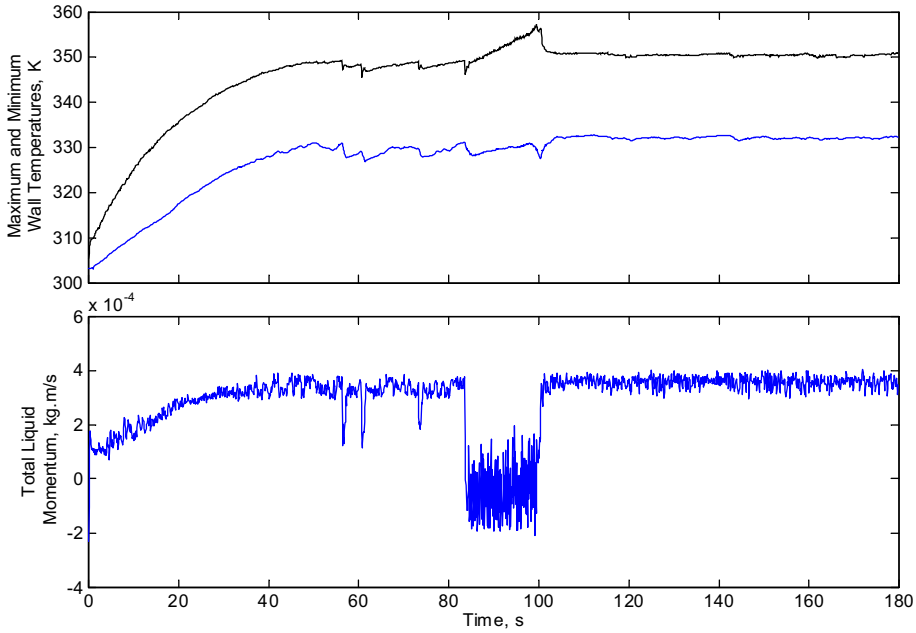

Fig. 8. Change in operation between circulatory and non-circulatory flow patterns (Case 11).

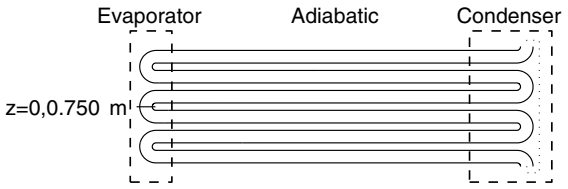

Fig. 9. Layout of a PHP: total length 75 cm, with 6 cm combined evaporator length, 12 cm combined condenser length and 57 cm adiabatic. The dashed line indicates the joining of two ends of the flow path to form a looped PHP.

or opposite direction. The model predicts similar behavior as shown in Fig. 8, where circulatory flow transitions to non-circulatory flow, and then back again to circulatory flow. The maximum wall temperature increases when circulation ceases, indicating the benefit of circulatory flow.

4.3. Flow pattern map

In this example, a map indicating oscillatory, circulatory, or stopped (device failure) flow patterns is generated with variations in two parameters: fill ratio and diameter profile. The PHP modeled has six parallel tubes. The layout is described in Fig. 9. Each parallel tube is 0.125 m in length. The evaporator and the condenser are in contact with each channel, and the total heat input rate is 60 W, distributed along the evaporator length. The second of each pair of parallel tubes may be a smaller size from case to case (as in Cases 2–14). The inclination angle is −90° or top heat mode. In each case for the flow map, the flow takes on one of three patterns: oscillatory, circulatory, or decaying.

With oscillatory flow, the liquid forms three slugs, one for each condenser section, and these slugs behave at steady state as in Case 20 of Fig. 10A. The number of slugs formed being equal to the number of condenser sections is in agreement with Shafii et al. [5]. The oscillation is indicated by the total liquid momentum, which ideally would average to zero over time. The time average for the period shown is less than 2% of the maximum absolute momentum.

Circulatory flow in top heat mode with the six parallel tube device is different from that seen in the two parallel tube device in bottom heat mode. With the two parallel tube device, circulation tends to be steady due to the buoyancy of vapor plugs. With six parallel tubes and top heat mode, circulation is mixed with oscillation. Fig. 10B shows the menisci positions and total liquid momentum as functions of time. While liquid slugs oscillate, smaller slugs break off and flow toward an adjacent slug, and this tends to occur in one direction. In Fig. 10B the movement of the slugs that break off tends to be upward or positive along the flow path. The total liquid momentum varies within a range that is mainly greater than zero, indicating net circulation. This is different from the flow observed in Fig. 6, where buoyancy tends to make the circulation more constant.

The flow in some cases decays and stops. Here, flow is stopped when slug movement ceases, and the maximum wall temperature steadily rises while the minimum wall temperature falls towards the ambient temperature.

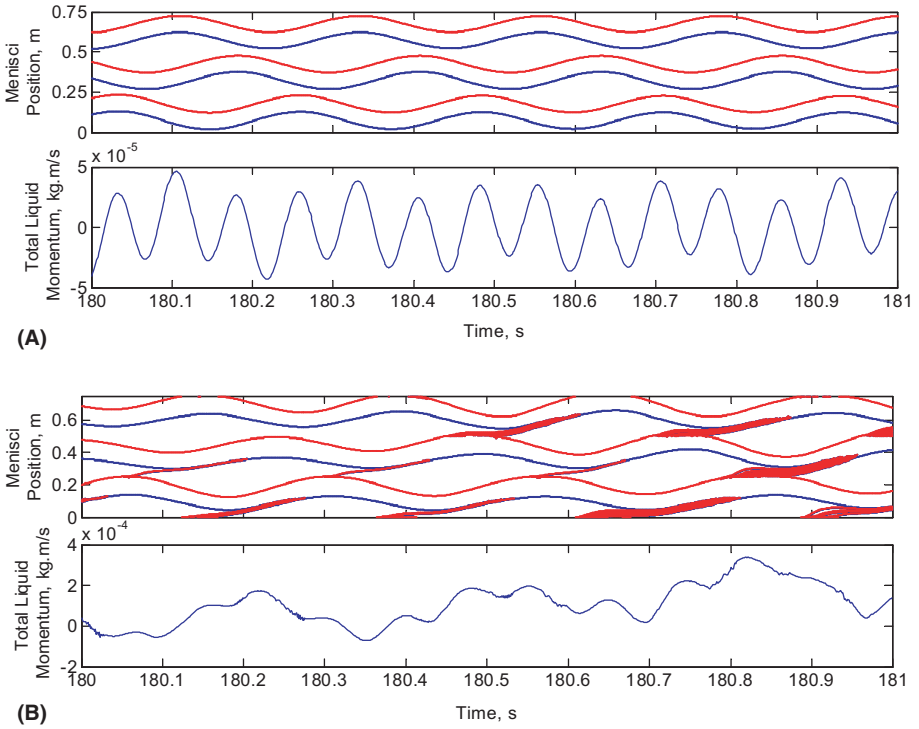

Fig. 10. Menisci positions and total liquid momentum for 1 s simulation time at steady state showing (A) oscillatory and (B) circulatory flow patterns (Cases 20 and 36, respectively).

Table 4
Flow pattern map

d, mm	γ							
	0.65	0.60	0.55	0.50	0.45	0.40	0.35	0.30
2.0/2.0	x	o	o	o	o	o	o	o
1.9/2.0			x	c	o	o	o	o
1.8/2.0				x	c	o	o	o
1.7/2.0				x	c	c	c	x
1.6/2.0					x	x	c	o
1.5/2.0						x	x	x

This indicates device failure. With the flow patterns defined, the flow map is presented (Table 4).

The map indicates trends in behavior as fill ratio and diameter profile change. Stopped flow is indicated by an "x", oscillatory: "o", and circulatory: "c". As tube diameter decreases, the maximum fill ratio allowable for the device to function also decreases, which may be due to viscous damping in the fluid or increased blocking of the condenser to vapor. Where the tube diameter is a uniform 2.0 mm, no circulatory flow takes place because of the symmetry in flow path geometry.

As the flow path geometry becomes less symmetric, and the tube diameter decreases for sections of the PHP, the likelihood of circulatory flow increases. A larger fill ratio also promotes circulatory flow in these asymmetric PHPs. Larger liquid slugs may be more likely to collide and give way from oscillatory flow to circulation. Further decrease in diameter increases the tendency toward device failure, as the flow becomes too restricted in the small diameter sections of the tube.

4.4. Effect of inclination angle and fill ratio

The effect of inclination angle on heat transfer differs with variation in other parameters including diameter profile and fill ratio. Results from Cases 16, 20, 36, and 44–55 show the dependence of heat transfer on inclination angles from bottom to top heat mode. The variation in steady state maximum and minimum wall temperatures coincides with apparent differences in the fluid flow. Fig. 11 is the rise of maximum and minimum wall temperatures to steady state for bottom and top heat modes. The curve for top heat mode is smoother than that for bottom heat mode. The smoother curve on top occurs due to the smooth oscillation of the liquid slugs. The curve on the bottom corresponds with the collision and formation of smaller slugs, and a more vigorous movement of the liquid. The merging and forming of slugs coincides with better heat transfer as indicated by the smaller temperature differential. The absence of collisions leads to a larger oscillation frequency. The

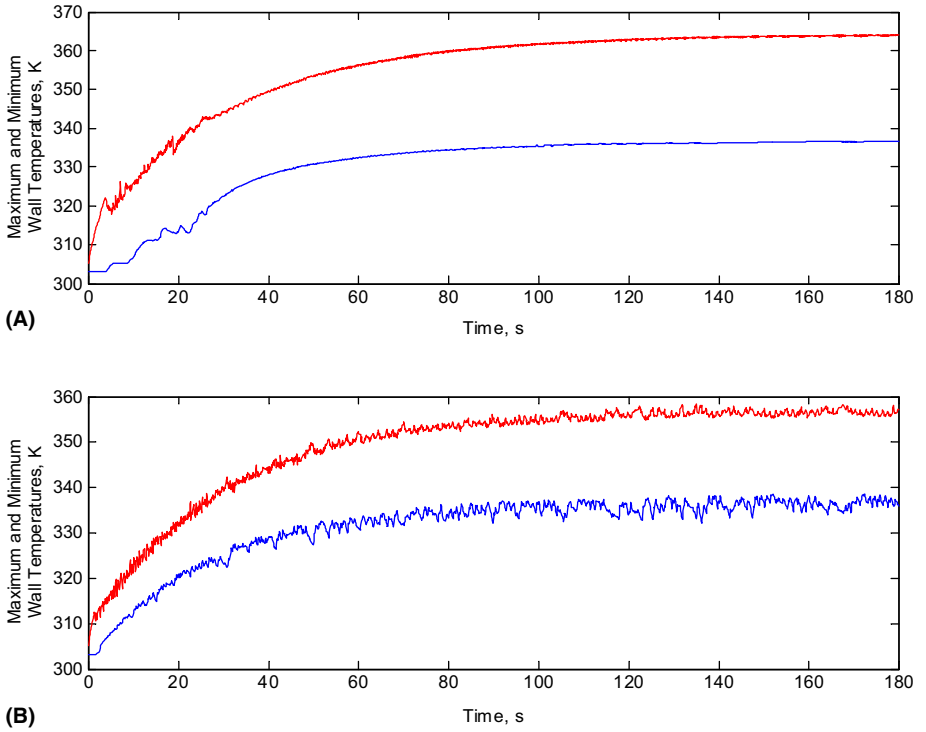

Fig. 11. Maximum and minimum wall temperature rise to steady state: (A) top heat mode (Case 16), (B) bottom heat mode (Case 47).

behavior of the remaining cases lies within the range of behavior described above.

For the set of cases with fill ratio $\gamma = 0.60$, the trend of average maximum wall temperature versus inclination angle is sharp. Fig. 12A shows the trend from top to bottom heat mode. Referring back to the flow map, operation at this fill ratio with the corresponding diameter nears device failure in top heat mode. These results qualitatively reflect experimental observations. Zuo et al. [2] reported that their PHP with sintered copper wick operated in both bottom and top heat modes, and top heat mode operation coincided as expected with a larger temperature differential between the evaporator and the condenser. The evaporator size reported is 1 cm^2, which is similar to what is modeled here. Other details, including diameter and condenser size were not reported, so a more direct comparison cannot be drawn.

With the same diameter profile and a $\gamma = 0.40$ fill ratio, there is less sensitivity to gravity, and heat transfer is generally better. With less liquid in the device, the cooling section is more accessible to vapor, allowing more condensation, which occurs with a higher heat transfer coefficient than with sensible heat transfer. With the wick in place, it is not necessary for liquid slugs to wet the entire evaporator section, so the evaporation rate is not reduced.

This section of results agrees in part with previously reported experimental results. Zuo et al. [12] report improved heat transfer when the fill ratio increases from 0.50 to 0.70, which is not the case in this model. The geometry of the experimental heat pipe is similar to that modeled here, but there are details of the experiment that are not provided: cooling section length, orientation, and how fill ratio was defined and determined with the inclusion of a wick. For the high heat fluxes tested experimentally, the assumption of slug flow in the model might not hold up, and the effect of conduction among parallel channels is also unknown. There is, however, greater agreement with other experimental results. Cai et al. [13] and Nishio [14] both report reduction in heat transfer performance for fill ratios above 40–50% in PHPs with water as a working fluid. These PHPs do not have a wick.

The set of cases with variation in channel diameter indicates that this configuration does not perform as well as with uniform diameter at the fill ratio of 40%. On the other hand, there is less sensitivity to gravity in the case where diameter varies. This may be a beneficial characteristic for end use, and a better combination of fill ratio and channel profile may be possible.

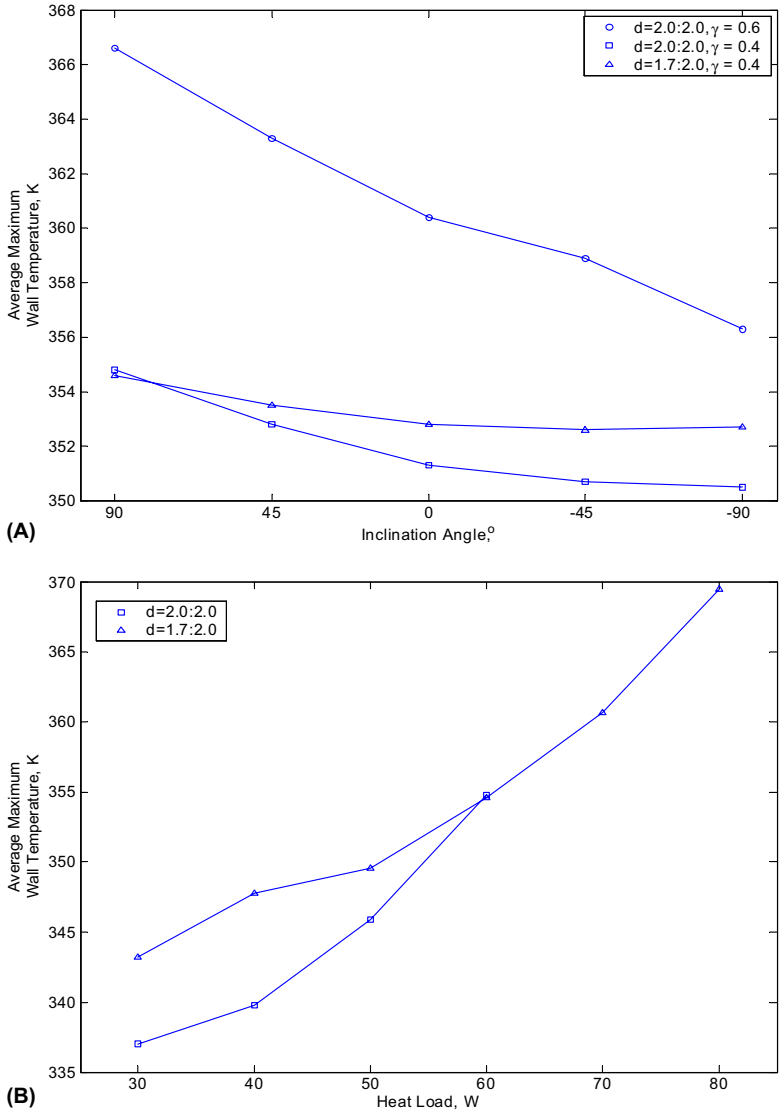

Fig. 12. Maximum wall temperatures averaged over 10 s at steady state versus: (A) inclination angle from top heat mode (−90°) to bottom heat mode (Cases 16, 20, 36, and 44–55), (B) heat load in top heat mode (−90°) (Cases 20, 36, and 65–72).

4.5. Effect of mean laminar Nusselt number on heat transfer

Due to the wide range in Nusselt number for laminar flow, the sensitivity of the heat transfer to Nusselt number is investigated. The Nusselt number can vary from 4.36 for laminar hydrodynamically and thermally developed flow with a constant wall heat flux to over 40 for undeveloped laminar flows [11]. Since the flow is unsteady and is subject to back and forth motion, the Nusselt number is likely to be greater than the 4.36 assumed in this analysis. The values of Nusselt number used in these two sets of cases include 4.36 and values between 10 and 30 with increments of 5. The two sets of cases cover oscillatory and circulatory flow patterns.

Variation in the mean Nusselt number for laminar flow has little effect on the cases simulated. It can be expected that the more the condenser is exposed to vapor, and since the condensation heat transfer coefficient is so much greater than that for laminar slug flow, the effect of changes in the Nusselt number for laminar flow would be smaller. For most cases the trend for maximum wall temperature decreases with increasing Nusselt number, but the entire range lies within 1.5 K. Variations in mean Nusselt number for laminar flow may have more effect in cases where the condenser section

does not come in contact with vapor, if flow can be sustained under such conditions.

4.6. Effect of heat load in top heat mode

The final two sets of cases describe how heat transfer performance can depend on heat load. One set of cases represents a constant diameter profile, and the other set a variable profile. Each has the same fill ratio of 40%. Heat loads beginning with 30 W and increased by increments of 10 W are simulated in top heat mode, until device failure occurs.

The results show better performance of the constant diameter profile heat pipe initially, but the variable diameter profile device was capable of higher heat loads. Fig. 12B shows the trends for the two case sets. Under 60 W the constant diameter profile PHP performs better, but it failed for the heat loads simulated above 60 W. The variable diameter device did not fail until 90 W was simulated. This extension of heat load capability may be a beneficial characteristic in some applications.

5. Conclusion

A model for a pulsating heat pipe with capillary wick and varying channel diameter has been presented. The model accounts for variation in the size of liquid slugs, circulation of the working fluid, the inclusion of a porous wick along the walls of the channel, and spatial variation in channel diameter. Results from the model are summarized as follows:

(1) The model results displayed similar trends with some published experimental data regarding fill ratio and inclination angle.
(2) Buoyant circulatory flow was predicted for a two parallel tube PHP operating in bottom heat (thermosyphon) mode. Reducing the diameter of one of the parallel tubes was simulated to augment circulation and heat transfer. Flow reversal, which has been observed by other investigators in experimental studies of such configurations, occurred in the simulations.
(3) It was demonstrated how the model could be used to produce a flow map of PHP operation, whether the flow be oscillatory, circulatory, or device failure.
(4) Variation in the Nusselt number for laminar slug flow was found to have little effect for the cases simulated.
(5) For configurations with more parallel tubes, varying the tube diameter profile resulted in less sensitivity to inclination angle and a larger range of heat load capability.
(6) Heat loads of up to 15 W per parallel tube were simulated for top heat mode.

Acknowledgement

Funding for this work was provided by US Army RDECOM Power & Energy IPT.

References

[1] R.L. Webb, Principles of Enhanced Heat Transfer, Wiley–Interscience, New York, 1994.
[2] Z.J. Zuo, M.T. North, K.L. Wert, High heat flux heat pipe mechanism for cooling of electronics, IEEE Trans. Components Packaging Technol. 24 (2) (2001) 220–225.
[3] K. Gi, F. Sato, S. Maezawa, Flow visualization experiment on oscillating heat pipe, in: Proceedings of the Eleventh International Heat Pipe Conference, Tokyo, Japan, 1999, pp. 149–153.
[4] S. Khandekar, M. Groll, An insight into thermo-hydrodynamic coupling in closed loop pulsating heat pipes, Int. J. Therm. Sci. 43 (1) (2004) 13–20.
[5] M.B. Shafii, A. Faghri, Y. Zhang, Thermal modeling of unlooped and looped pulsating heat pipes, J. Heat Transfer 123 (2001) 1159–1172.
[6] H. Akachi, Looped Capillary Heat Pipe, Japanese Patent Hei6-97147, 1994.
[7] X. Geng, H. Yuan, H.N. Oguz, A. Prosperetti, Bubble-based micropump for electrically conducting liquids, J. Micromech. Microeng. 11 (2001) 270–276.
[8] F.M. White, Viscous Fluid Flow, McGraw-Hill, New York, 1974.
[9] E. Begg, B. Holley, A. Faghri, Condensation heat transfer and pressure drop measurements in miniature horizontal tubes with low mass flux rates, J. Enhanced Heat Transfer 10 (3) (2003) 335–354.
[10] A. Faghri, Heat Pipe Science and Technology, Taylor & Francis, Washington, DC, 1995.
[11] A. Bejan, Convection Heat Transfer, Wiley–Interscience, New York, 1995.
[12] Z.J. Zuo, M.T. North, L. Ray, Combined pulsating and capillary heat pipe mechanism for cooling of high heat flux electronics, in: Proceedings of the ASME HTD Conference, Nashville, TN, 1999, pp. 2237–2243.
[13] Q. Cai, R. Chen, C. Chen, An investigation of evaporation, boiling, and heat transport performance in a pulsating heat pipe, in: Proceedings of ASME IMECE 2002, New Orleans, LA, 2002.
[14] S. Nishio, Oscillatory-flow heat-transport device (forced oscillatory flow type and bubble driven type), in: Proceedings of the Eleventh International Heat Pipe Conference, Tokyo, Japan, 1999, pp. 39–49.